Soft transition between subcritical and supercritical currents through intermittent cascading interfacial instabilities

Jorge Salinas[a,1], S. Balachandar[a], Mrugesh Shringarpure[b], Juan Fedele[b], David Hoyal[b], and Mariano Cantero[c,d,e]

[a]Department of Mechanical and Aerospace Engineering, University of Florida, Gainesville, FL 32611; [b]Process Stratigraphy, Reservoir Systems, ExxonMobil Upstream Research Company, Houston, TX 77389; [c]Instituto Balseiro, Universidad Nacional de Cuyo, San Carlos de Bariloche, 8400, Argentina; [d]Centro Atómico Bariloche, Comisión Nacional de Energía Atómica, San Carlos de Bariloche, 8400, Argentina; and [e]Consejo Nacional de Investigaciones Científicas y Técnicas, San Carlos de Bariloche, 8400, Argentina

Edited by Michael Manga, University of California, Berkeley, CA, and approved June 23, 2020 (received for review May 8, 2020)

Long-running gravity currents are flows that are submerged beneath a deep layer of quiescent fluid and they travel over long distances along inclined or horizontal surfaces. They are driven by the density difference between the current and the clear ambient fluid above. In this work we present results on highly resolved direct numerical simulations of turbid underflows that involve nearly 1 billion degrees of freedom. We assess the effect of bed slope on the flow statistics. We explore the turbulence dynamics of the interface in the classical sub- and supercritical regimes. We investigate the structure of interfacial turbulence and its relation to the turbulence statistic. A transcritical regime is identified where intermittent cascading interfacial instabilities appear. We investigate how departure from the self-sustaining equilibrium state may be the mechanism responsible for this cyclic evolution of the transcritical regime.

turbid underflow | turbidity current | gravity current | turbulence | DNS

Long-running subaqueous gravity currents are driven by the density difference between the heavy fluid and the clear water above it. This density difference can be the result of salinity of the current's fluid or difference in temperature. Moreover, sediment-laden turbidity currents can be modeled as density currents in the limit where very fine, noncohesive sediment is suspended in the current. This limit is the focus of the present work. These energetic turbid underflows travel along the oceanic floor generating submarine channel systems (1, 2), where they interact with the sediment bed at the bottom by eroding and depositing sediment and with the clear fluid above by entraining ambient water into the current (3). Near-bed turbulence is of essence in these sediment-laden flows to keep the sediments in suspension. These currents can travel hundreds of kilometers and last for several days (4–6). Direct monitoring of these energetic events and the resulting deposits is an ongoing challenge. An enlightening discussion on the key future research directions on turbidity currents and their deposits is presented in ref. 7.

For these flows, two different flow regimes are well recognized: the supercritical regime where interfacial disturbances cannot travel upstream versus the subcritical regime where the velocity of the current is sufficiently low that disturbances can travel upstream. These two regimes are parametrically demarcated by the densimetric Froude Fr or equivalently the bulk Richardson number Ri of unity (8). The densimetric Froude number Fr is defined as the ratio between inertial and buoyancy effects and can be computed as $Fr = (\frac{1}{h_u}\int_0^\infty \overline{u}\,dz)/(\int_0^\infty \overline{c}\,dz/\tan\theta)^{1/2}$, where $\overline{u}$ and $\overline{c}$ are the averaged streamwise velocity and concentration, respectively, and h_u is the top edge of the current where streamwise velocity is negligible. Note that the bulk Richardson number can be computed as $Ri = 1/Fr^2 = \int_0^\infty \overline{c}\,dz/(\tan\theta(\frac{1}{h_u}\int_0^\infty \overline{u}\,dz)^2)$. When the Fr of a current flowing down a steep (or gentle) slope is sufficiently greater (or less) than unity, it can remain supercritical (or subcritical) and slowly evolve over very long distances. Such a slow evolution over very long distances is possible due to near equilibrium between the excess weight of suspended sediments along the downslope direction and the total drag at both the bottom and the top of the current. At equilibrium, a supercritical current is characterized by strong energetic mixing at the interface between the current and the ambient fluid and a velocity profile (Fig. 1*A*) that resembles the nose-down shape of a wall jet (9, 10). As a result of strong mixing by turbulence at both the interface (above the velocity maximum) and the wall region (below the velocity maximum), the sediment concentration follows a Rousian profile (11). At equilibrium, a subcritical current is characterized by a stable interface with little mixing between the current and the ambient (Fig. 1*B*) and a nose-up velocity profile (12, 13). The sediment concentration in an equilibrium subcritical current is constant with height and is capped by a lutocline of abrupt drop in sediment concentration (12).

In this work we report on the existence of an intermediate transcritical regime through which the current undergoes a soft parametric transition between the subcritical and supercritical regimes. We study the properties of the hitherto unexplored transcritical regime through direct numerical simulations of heavier-than-ambient underflows (Fig. 1*C*). The nature of

Significance

Gravity currents are predominantly horizontal flows driven by the density difference between the current's fluid and the ambient fluid above. The two well-established flow regimes are the supercritical and subcritical regimes. We report on the existence of an intermediate transcritical regime where the flow along the interface undergoes a cyclical transition between quiescent and highly intermittent turbulent states. While the current slowly evolves in the subcritical and supercritical regimes in a near self-similar manner (akin to dynamics near a stable fixed point), the transcritical current with its unique cyclical evolution exhibits a limit-cycle–like behavior. This phenomenon has hitherto been unreported, since it requires highly resolved simulations over very long streamwise length involving about 1 billion grid points.

Author contributions: S.B., M.S., J.F., D.H., and M.C. designed research; J.S. performed research; J.S. analyzed data; and J.S. and S.B. wrote the paper.

The authors declare no competing interest.

This article is a PNAS Direct Submission.

Data deposition: Simulation data are have been deposited to Open Science Framework, available at https://osf.io/x9vw4/.

[1]To whom correspondence may be addressed. Email: josalinas@ufl.edu.

This article contains supporting information online at https://www.pnas.org/lookup/suppl/doi:10.1073/pnas.2008959117/-/DCSupplemental.

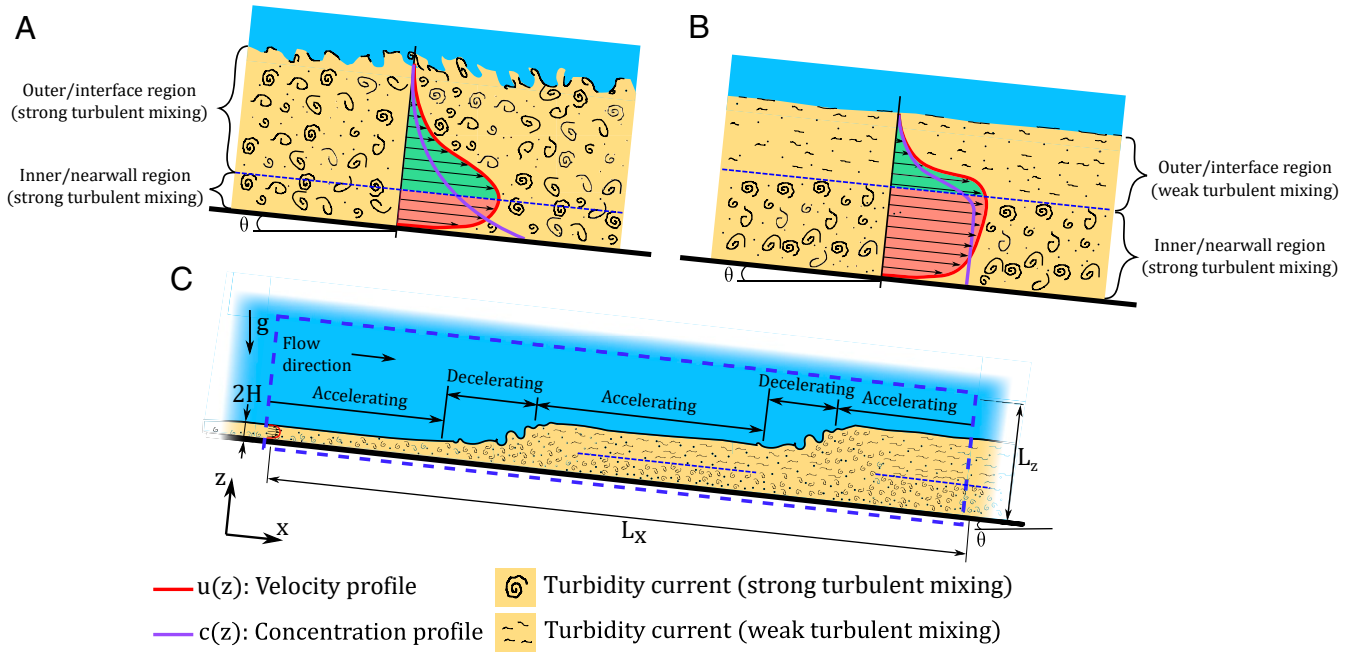

Fig. 1. (*A* and *B*) Schematic representation of a turbidity current in the (*A*) supercritical regime and (*B*) subcritical regime. (*C*) Schematic representation of cascading spatiotemporal instabilities in the turbidity current.

turbulence at the interface between the current and the ambient is of particular interest as it appears to involve a cascading sequence of laminar-to-turbulent transitions through intermittent instabilities followed by slow acceleration back to the laminar state, and so on (Fig. 1*C*). The challenging aspect of this intermediate scenario is that it requires observation (or simulation) over a current length many orders of magnitude greater than the height. Unlike the equilibrium supercritical and subcritical, in the transcritical state, the buoyancy force and total drag are never in balance. This departure from local equilibrium is the source of periodic acceleration and deceleration of the current and an intermittent turbulent state of the interface. Furthermore, the present results suggest that the transition between the subcritical and supercritical regimes is not as sharp (13) and that the transcritical behavior may exist over an intermediate range of slope and Fr around unity (14, 15).

Although the present study has identified the transcritical regime in the context of a constant intermediate slope, it can be conjectured that a similar behavior occurs even in the case of forced transition from the supercritical to the subcritical regime following a steep-to-gradual slope break (16–19). In this case the current transitions to the subcritical regime through an internal (subaqueous) hydraulic jump. In the present context of a transcritical flow as well, the repeated transition between the supercritical and the subcritical regime appears to display features of internal hydraulic jumps (20, 21).

The alternating pattern of long reaches of laminar and turbulent interfaces greatly influences wall turbulence and results in periodic patches of enhanced deposition and erosion. Several works have studied the formation of upstream-migrating cyclic steps in subaerial (22, 23) and subaqueous (23, 24) flows. It can be conjectured that the mechanisms responsible of such cyclic steps are similar to those observed in the present study.

Simulation Details

We report on three direct numerical simulations of dilute turbidity currents flowing down a sloping bed of constant inclination $\theta = 0.29°$, $0.72°$, and $2.86°$, which are respectively in the subcritical, transcritical, and supercritical regimes. We study the particular limit where sediment particles are noncohesive, but fine, which allows us to isolate the effect of slope by ignoring the effects of settling and inertia of particles (i.e., we consider the limit of zero settling velocity and zero Stokes number). The inlet bulk Richardson numbers are $Ri_{in} = 1.77$, 0.75, and 0.18, for the subcritical, transcritical, and supercritical cases, respectively. The results are nondimensionalized with the half-height H of the inlet as the length scale (Fig. 1) and the average inlet concentration c_v as the concentration scale. The velocity scale is given by $u_* = \sqrt{g' H}$ (25). Here $g' = Rc_v g \sin\theta$ is the reduced gravity with g being the acceleration due to gravity, and $R = \rho_s/\rho_f - 1$, where the sediment and the clear fluid are of density ρ_s and ρ_f, respectively. The excess weight due to the sediment field in the streamwise direction drives the flow, while the excess weight in the bed-normal direction is the measure of bulk stratification. There are two dimensionless parameters: the shear Reynolds number $Re_\tau = u_* H/\nu$ and the Schmidt number $Sc = \nu/\kappa$. Here ν is the kinematic viscosity and κ is the sediment diffusivity.

The three simulations are performed at a fixed $Re_\tau = 180$ and $Sc = 1$ (26). The current travels downslope in a very long domain of length $L_x = 96\pi$, while entraining ambient fluid from above. The height and the width of the computational domain are $L_z = 20$ and $L_y = 8\pi/3$, which allow unhindered entrainment.

Structure of Super-, Sub-, and Transcritical Regimes

Fig. 2 shows the interface between the current and the ambient as an iso-surface of concentration $c = 0.01$ plotted only over half of the domain (shaded light brown). Also shown is the iso-surface of swirling strength $\lambda_{ci} = 2$ (27, 28), for all cases at one time instant. The iso-surface of swirling strength is colored by the wall normal position z and it identifies intense turbulent structures that are typically in the form of hairpin and quasi-streamwise vortices in the near-wall and interface regions (29).

The higher slope of case 1 results in a supercritical flow and both the interface and the near-wall regions are intensely turbulent. The interface is populated with many hairpin vortices that are oriented opposite to the flow and deform the concentration field by transporting sediment into the ambient fluid above. This

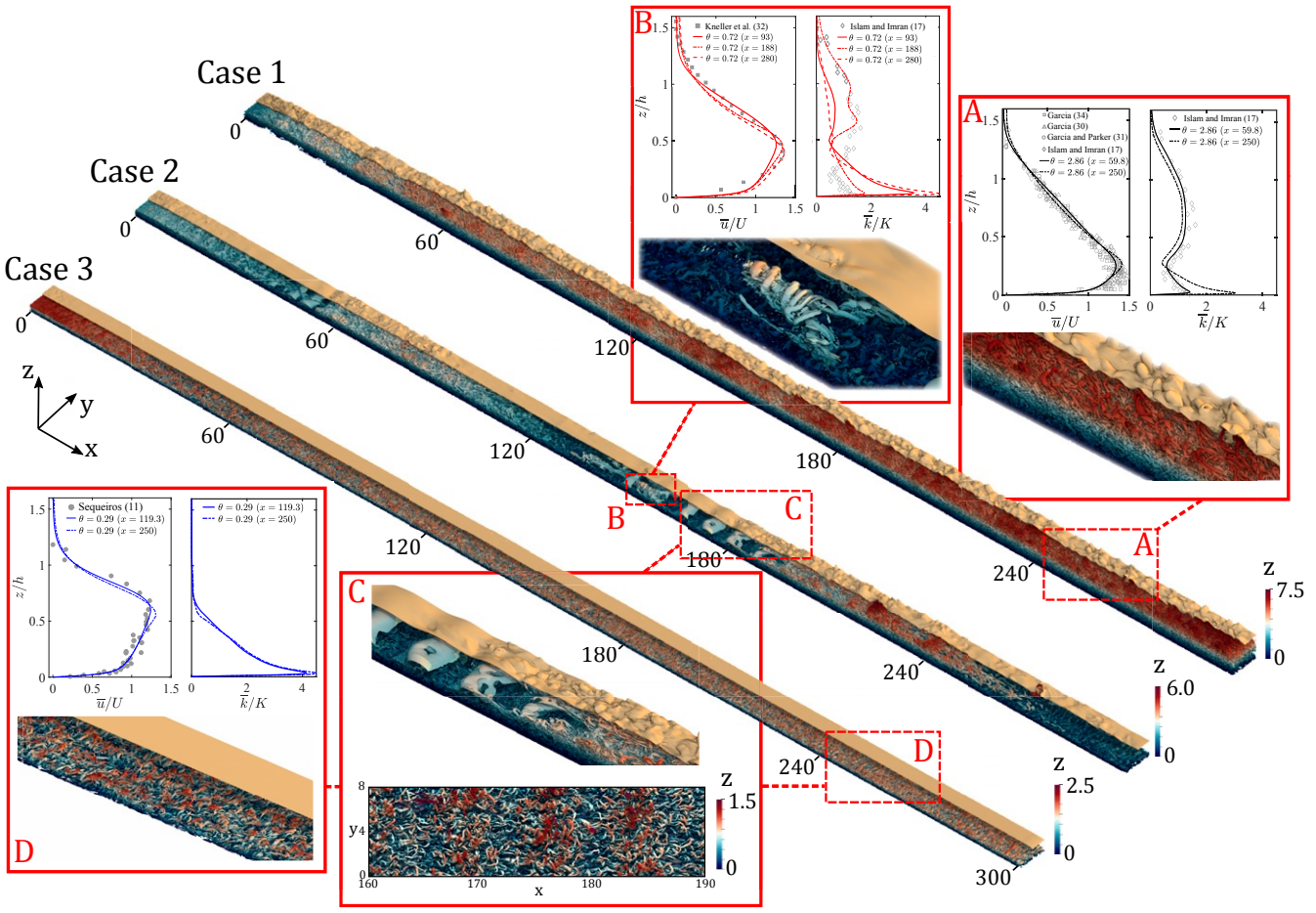

Fig. 2. (*A–D*) Iso-surface of concentration $c = 0.01$ (light brown) for half of the domain with iso-surface of swirling strength $\lambda_{ci} = 2$, for all cases at one time instant in the statistically steady state [Sequeiros (11); Islam and Imran (17); Garcia (30); García and Parker (31); Kneller et al. (32); Garcia (34)]. The iso-surface of swirling strength is colored by the wall normal position *z*. Case 1, $\theta = 2.86°$; case 2, $\theta = 0.72°$; case 3, $\theta = 0.29°$.

correlation between vortical and concentration structures can be seen in Fig. 2*A*, where a closeup shows sediment-laden tongue-like instabilities that penetrate into the clear fluid, shaped by the hairpin vortices (13, 33). Fig. 2*A* also shows profiles of normalized streamwise velocity as a function of z/h (Eq. **2**) at two different downstream locations: at $x = 59.8$ when a normal condition is achieved (13) and far downstream at $x = 250$. These results are averaged over time and along the spanwise y direction and denoted with an overbar $(\overline{\cdot})$, while perturbations from the mean are denoted by a prime $(\cdot)'$. We also present experimental data from refs. 17, 30, 31, and 34 in the supercritical regime. The velocity maximum increases as the current travels downstream and the bed-normal location slightly increases. The velocity profile resembles that of a wall jet characterized by a sharp peak that is close to the bottom boundary and a near linear decrease in velocity above the peak. The scaled turbulent kinetic energy (TKE) $(\overline{k} = \frac{1}{2}\overline{u_i' u_i'})$ and the corresponding experimental measurements are also shown (Eq. **2**). There are two local maxima in case 1: one close to the bed at $z/h \approx 0.05$ and one at the interface ($z/h \approx 0.7$). The bottom maximum increases as the current travels downstream, while the top maximum does not change significantly.

The subcritical case 3 exhibits a stable interface. However, the near-wall region below the velocity maximum (Fig. 2*D*) is populated by hairpin vortices and resembles a turbulent boundary layer (35). Again, the velocity maximum increases from the location of normal velocity (x = 119.3) to the far downstream location of $x = 250$, but the bed-normal location of the maximum moves closer to the bottom bed. Furthermore, we find a good agreement with experimental data from ref. 11 for density currents in the subcritical regime. The TKE profiles show a single peak in the near-wall region, which slightly increases as the current travels downstream.

The interesting transcritical behavior of case 2 shows spatially intermittent turbulent structures at the interface. In the region $90 \lessapprox x \lessapprox 150$ the interface is stable, as evidenced by the almost flat iso-surface. At $x \approx 150$ instabilities start to grow and packets of Ω-shaped vortices appear (Fig. 2*B*). Downstream from this region ($150 \lessapprox x \lessapprox 210$), coherent interfacial instabilities appear, which are well correlated with the wavy structure of the interface (Fig. 2*C*). After $x \approx 210$, the turbulent structures stretch and break up into smaller structures. Thus, over the length $210 \lessapprox x \lessapprox 250$ the height of the current rapidly increases. The interface stabilizes for $x \gtrapprox 250$ and the current continues to slowly accelerate and eventually becomes unstable again. Over the length $0 \geq x \geq 300$ transitions through spatially and temporally intermittent interfacial instabilities can be observed at two locations ($x \approx 50$ and $x \approx 150$). This cyclic behavior of stable interface, growth of coherent instabilities, stretching and breakup of the vortical structures, and restabilization of the interface is observed many more times in an even longer simulation of length $L_x \approx 900$ (*SI Appendix*, Fig. S1).

While the internal structures of the super- and subcritical currents of cases 1 and 3 support their slow near-equilibrium

evolution, it can be seen that the nonequilibrium of the internal structure of the transcritical current is the source of its cyclic evolution. In Fig. 2*B*, the maximum velocity of the transcritical case is located at about $z/h \approx 0.5$, in between those of cases 1 and 3. We see good agreement with numerical results obtained by ref. 32. The TKE profiles before and after the second onset of instabilities (at $x = 93$ and 280) are also at an intermediate state between cases 1 and 3. Furthermore, in the region of instabilities ($x = 188$), the near-wall TKE decreases, while it increases at the interface to values on the order of case 1 and experimental data from ref. 17. From these we see that case 2 starts at $x = 93$ with a TKE profile that is in between those of equilibrium supercritical and subcritical regimes, goes through interfacial instabilities where TKE is similar to that of an equilibrium supercritical current, and then transitions to a profile closer to that of an equilibrium subcritical current. However, the velocity profile does not change significantly. This suggests that the classical nose-down/nose-up description of velocity correctly identifies the super/subcritical regime and internal distribution of turbulence only under near-equilibrium evolution.

Depth-Averaged and Bulk Statistics

Following the works of refs. 14 and 36, the depth-averaged streamwise velocity U, concentration C, turbulent kinetic energy K, and current thickness h are defined by further averaging in the wall-normal direction:

$$U = \frac{\int_0^\infty \overline{u}^2\, dz}{\int_0^\infty \overline{u}\, dz}, \quad C = \frac{\int_0^\infty \overline{u}\,\overline{c}\, dz}{\int_0^\infty \overline{u}\, dz}, \qquad [1]$$

$$K = \frac{\int_0^\infty \overline{u}\,\overline{k}\, dz}{\int_0^\infty \overline{u}\, dz}, \quad h = \frac{(\int_0^\infty \overline{u}\, dz)^2}{\int_0^\infty \overline{u}^2\, dz}. \qquad [2]$$

We define the bulk Reynolds number $Re = Re_\tau Uh$. Fig. 3*A* shows $U \approx 16$ at the inlet, which quickly evolves to a lower/higher value in the super/subcritical cases. In cases 1 and 3, the current reaches a normal condition where the flow neither locally accelerates nor decelerates (i.e., $dU/dx = 0$). Downstream from the normal condition the current slowly accelerates. In contrast, case 2 evolves through multiple normal conditions and the amplitude of oscillation of U seems to increase. Fig. 3*B* shows the depth-averaged concentration C to steadily decrease from its initial value of unity and correspondingly in Fig. 3*C* the sediment layer thickness h continues to increase as a function of x. The rate of increase in h and correspondingly the rate of decrease in C increase with the slope of the bed. In other words, a supercritical current vigorously mixes with the ambient, resulting in a faster growth of its height and rapid dilution of sediment concentration. A cyclic behavior is observed in the transcritical case 2, where bursts of rapid increase in current height are observed at $x \approx 50$ and $x \approx 175$ corresponding to locations of intermittent instabilities and turbulence.

Fig. 3*D* presents the bulk Reynolds number Re as a function of bulk Richardson number Ri for the three cases. Following refs. 37 and 38, we visually identify four states of the interface between the ambient layer and the current: V, viscous steady flow, with a lutocline at the interface (green); W, finite-amplitude wave propagation (blue); I, intermittent turbulence (red); and T, sustained turbulence with interfacial mixing layer (black). These stages are also identified in Fig. 3*A* with the same color scheme as in Fig. 3*D*. In the viscous "V" state the interface visually lacks undulations, although nonzero turbulence fluctuations are present. This region is akin to the viscous sublayer of a viscous boundary layer. As the current travels downstream, Re increases with increasing x, and thus the evolution of each current can be tracked from the bottom of the curve to the top. Several intermediate x locations are marked. In the supercritical case 1, Ri increases until $x \approx 50$ where $dU/dx \approx 0$, after which it decreases. In the subcritical case 3, Ri mainly decreases as the current travels downstream. It must be stressed that the near-wall region of the flow remains turbulent even though the interface is laminar. In the transcritical case 2, Ri evolves in an oscillatory manner and in the process crosses the critical value of $Ri = 1$ (or $Fr = 1$) several times.

To assist our interpretation, Fig. 4 *A*, *C*, and *E* shows the instantaneous span-averaged concentration field for the three cases. White contours correspond to $c = 0.01$. Plots are stretched in the wall-normal direction for better visualization. Clear evidence of strong interfacial turbulence is observed in the supercritical case 1 with the current being in the T state over the entire length. Downstream of the inlet, stratification effects initially increase (as indicated by increasing Ri) and then steadily decrease. The interface in the subcritical case 3 presents no shear-induced instabilities as a result of strong stratification (V state; Fig. 3*D*). The transcritical case 2 presents episodic instabilities and turbulence at the interface. Two such episodes start at $x \approx 40$ and $x \approx 150$ as instabilities (W state), which quickly break into an intermittent turbulent patch (I state), which is sustained

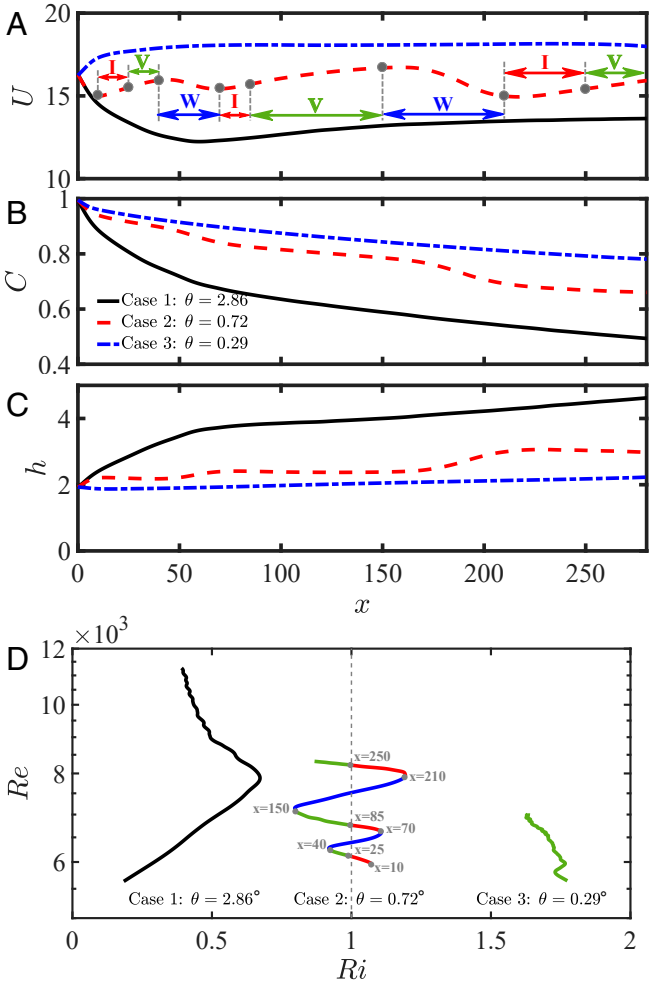

Fig. 3. (*A*–*C*) Depth-averaged (*A*) streamwise velocity *U*, (*B*) concentration *C*, and (*C*) layer thickness *h*, as a function of downstream location *x*. (*D*) Bulk Reynolds *Re* as a function of bulk Richardson number *Ri*: V (green), viscous regime; W (blue), finite-amplitude waves propagating downstream; I (red), spatio-temporally intermittent turbulence; and T (black), steadily sustained turbulence. Vertical dashed line denotes critical $Ri = 1$.

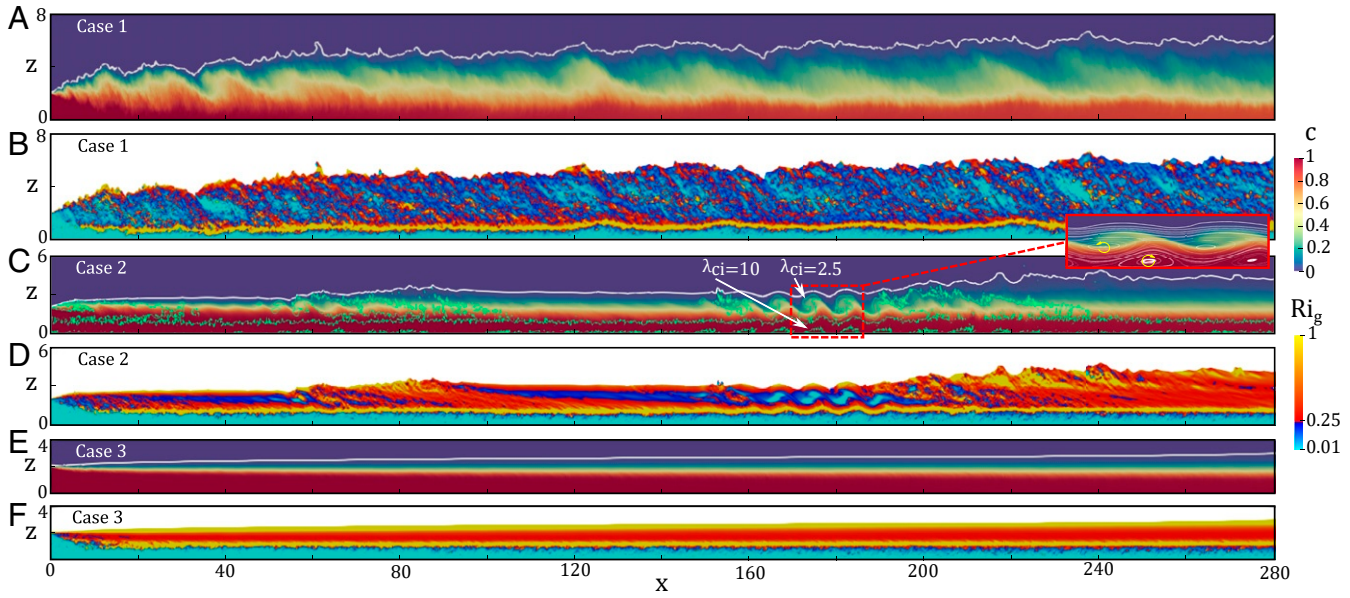

Fig. 4. (*A*, *C*, and *E*) Spanwise averaged concentration field at one instant in time in the statistically steady-state regime for cases 1 (*A*), 2 (*C*), and 3 (*E*). White contours correspond to $c = 0.01$. (*B*, *D*, and *F*) Spanwise averaged gradient Richardson number at one instant in time in the statistically steady-state regime for cases 1 (*B*), 2 (*D*), and 3 (*F*). Wall-normal axis is stretched for better visualization.

only over a limited extent and the flow reverts back to the viscous V state farther downstream. The regions of W and I states are well correlated with the rapid increase in the height of the current and the bulk Reynolds number. From Fig. 3*D* it can be seen that the viscous state follows after the Ri of the current has increased above unity, while instability and intermittent turbulence follow a period of Ri being less than unity. This phase lag is indicative of the persistent nonequilibrium of the current. More specifically, the V state evolves from the critical state $Ri \approx 1$ to a local minimum of Ri, the W state from a local minimum to a local maximum, and the I state from a local maximum to the critical state $Ri \approx 1$.

The near-wall region of the flow remains turbulent over the entire length; however, the large-scale instability-induced circulations at the interface significantly influence the near-bed region in the W state. Fig. 4 *C*, *Inset* shows a detailed view of case 2 at $x \approx 180$, where the white contours are streamlines of perturbation velocity. The yellow circular arrows show counterclockwise vortices at the interface and near-wall clockwise vortices in between. Their effect on near-wall turbulence can be seen in the contours of λ_{ci} presented in Fig. 4*C* (green contours), where packets of strong hairpin vortices with their head up until the velocity maximum are found in between interfacial coherent vortices in Fig. 2*C*. Directly below the interfacial vortices the hairpins are fewer and weaker. A careful look at the supercritical flow also reveals the presence of counterclockwise vortices at the interface along with clockwise near-wall vortices. The key difference is that the streamwise size of the vortices is much longer in the supercritical current.

The nature of cascading instability of the transcritical case is more evident in the plot of gradient Richardson number, which is defined as $Ri_g = -(\partial \overline{c}/\partial z)/(\tan\theta(\partial \overline{u}/\partial z)^2)$. Fig. 4 *B*, *D*, and *F* shows the instantaneous span-averaged gradient Richardson number for the three cases. Marked by a blue–red jump in color is the critical value of $Ri_g = 0.25$ (32, 39). In the supercritical case 1, Ri_g remains on average less than 0.25 both above and below the velocity maximum, which explains sustained vigorous turbulence (T state). In the subcritical case 3, $Ri_g > 0.25$ above the velocity maximum with little variation along the streamwise direction, confirming hindered interfacial mixing (V state). Below the velocity maximum Ri_g is below 0.25, thus maintaining near-wall turbulence. The same was observed in ref. 32, where they concluded that turbidity currents on small slopes driven by fine sediment have a stable interface (no shear-induced instabilities). In the transcritical case 2 (Fig. 4*D*), $Ri_g > 0.25$ above the velocity maximum at $x \approx 85$ and $x \gtrapprox 250$ (V state) after the rapid increase in height due to intermittent turbulence. However, a thin layer of blue indicating $Ri_g < 0.25$ initiates near the top of the current around $x \approx 90$, grows in thickness, and moves into the current downstream. In Fig. 3*D* the V state identifies the region where the interface is flat. Nevertheless, instabilities grow below the interface until it becomes unstable (W state). Associated growth of vortices, development of strong interfacial instability, and enhanced TKE can be observed downstream of $x = 150$ (W and I states). Below the velocity maximum, Ri_g remains below 0.25 and the wall region of the transcritical flow is turbulent over the entire length. However, the nature of wall turbulence is strongly modulated by the alternating laminar and turbulent states of the interface.

Discussion

A mechanistic explanation of the transcritical behavior can be offered based on the depth-averaged momentum balance

$$Ch \approx C_D U^2 + e_w U^2 + Uh\frac{dU}{dx} + \frac{1}{2\tan\theta}\frac{dCh^2}{dx}, \qquad [3]$$

where C_D is the basal drag coefficient and e_w is the entrainment coefficient at the interface (36). The left-hand side corresponds to the net streamwise force due to suspended sediment. In the present simulations, the total amount of sediment is conserved (i.e., $\int_0^{L_z} \overline{c}\,dz = 2$ at all times), and as a result we obtain $Ch \approx 2$. This momentum source is balanced by the four terms on the right-hand side: 1) basal drag at the bottom of the current, 2) interfacial drag which is the momentum needed to increase the velocity of the entrained fluid from the quiescent condition to the velocity of the current, 3) change in the streamwise momentum of the current, and 4) change in the potential energy of the current. In a long-running near-equilibrium supercritical current

the momentum source is balanced by all four mechanisms. In a long-running near-equilibrium subcritical current, the effects of interfacial mixing, streamwise acceleration, and change in potential energy are negligible. As a result, the momentum source is primarily balanced by basal drag.

In contrast, a transcritical current does not reach a fixed-point equilibrium, but evolves in a cyclical pattern. Upstream of $x = 40$ (V state in Fig. 3*D*) the interface is stable and accordingly the height of the current remains nearly a constant. There is minimal interfacial drag and little change in potential energy. However, the momentum source is not entirely balanced by basal drag and therefore the current accelerates. With this increase in the current's inertia, both bulk and gradient Richardson numbers steadily decrease (e.g., Ri decreases from 1.1 to 0.9). The interface can no longer remain stable after $x = 40$—interfacial vortices grow and break down to generate interfacial turbulence. With the rapid increase in the height for $50 \lessapprox x \lessapprox 85$ (W and I states), the momentum source is overbalanced by basal drag, interfacial mixing, and increase in potential energy. Thus, the current decelerates and accordingly Ri increases and most importantly Ri_g at the interface increases above 0.25. With interfacial stability reestablished, the current evolves at a near constant height over $85 \lessapprox x \lessapprox 150$ and the cycle repeats.

For the above limit-cycle equilibrium to exist, at no time the transcritical current fully resembles an equilibrium supercritical or a subcritical current. For example, at $x = 30$ and 140, even though the interface is quiet, Ri is less than unity, which is characteristic of a supercritical regime. Similarly, at $x = 75$ and 210, although the interface is highly unstable like a supercritical current, Ri is larger than unity and the current shows subcritical-like characteristics. This phase shift between the nature of the interface and the internal structure is instrumental for self-induced cyclic evolution.

While the interfacial vortices advect downstream at their phase velocity, the locations of the spatiotemporal instabilities are nearly frozen; i.e., the group velocity of the interfacial turbulent pockets is zero. The spacing between the first two onsets of interfacial instabilities is observed to be about 60 current heights. The longer simulation shows the spacing to be about 66 and 140 current heights, between the second-to-third and third-to-fourth instabilities. We note that the spacing between the interfacial turbulent patches will increase with decreasing slope and will eventually become very large with a smooth turbulence-free interface corresponding to a subcritical current. In fact, two different potential scenarios can be conjectured from Fig. 3. First, the oscillations seen for the transcritical case 2 might decrease after a long evolution and the current might reach a quasi-equilibrium state. On the other hand, if the slow decrease of Ri in case 3 were to continue after a long downstream distance, when Ri approaches unity, the current could become transcritical and continue to evolve in a cyclical manner.

Although not simulated, the potential effect of cyclic behavior of the transcritical regime on sediment erosion and deposition can be inferred by looking at the basal shear stress τ_w presented in Fig. 5. The enhanced basal shear just before the onset of the spatiotemporal instabilities (i.e., $x \approx 150$) can lead to increased local sediment erosion, while the lower current velocity and absence of interfacial turbulence in the postinstability state (i.e., $x \approx 210$) can contribute to enhanced deposition. Several past studies (23, 40) have demonstrated the existence of similar repeated transitions from the supercritical to the subcritical state and back again (cyclic steps), both in subaerial and in subaqueous contexts. They postulate the coexistence of simultaneous cyclical variation in both the current and the bedform. In contrast, the present study demonstrates the possibility of cyclical variation in the current, in the absence of any bedform. Here it should be emphasized that in the transcritical regime,

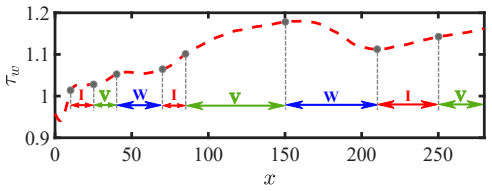

Fig. 5. Basal shear stress τ_w as a function of downstream location x for the transcritical case 2: V (green), viscous regime; W (blue), finite-amplitude waves propagating downstream; and I (red), spatio-temporally intermittent turbulence.

the states of the interface in the supercritical and subcritical states are different from their classical self-similar forms. In the supercritical state the interface is quiet while after transition to the subcritical state the interface becomes turbulent. As a result, this transition from supercritical to subcritical state is not through a hydraulic jump, but involves onset of instabilities and transition.

Unambiguous observational evidence is yet to be gathered but we speculate that, due to comparable spatial scales of development, the instabilities described in this work could be in principle linked to the origin of large-scale bedforms. Sediment waves are observed commonly in the sea floor or preserved in the sedimentary column and are typically associated with the action of both turbidity and other density flows (with hundreds of meters to few kilometers wavelength). The spacing between the first two instabilities in the transcritical regime is observed to be about 60 current heights. The longer simulation shows the spacing to somewhat increase between the second-to-third and third-to-fourth instabilities. For a current height of $O(100)$ meters, the spacing between the instabilities is consistent with the sediment wave observations. However, we emphasize the need for experimental testing and verification, since reported experimental and field measurements suggest that other types of instabilities, along with morphodynamic feedback between flow and sediment transport, might also be responsible for the formation and development of upper-regime (supercritical) bedforms under gravity flows (41, 42).

Materials and Methods

We perform the simulations using a highly scalable, higher-order spectral element solver (43, 44) that solves the incompressible Navier–Stokes equations together with a transport equation for the concentration field. The domain is discretized using $336 \times 15 \times 44$ hexahedral elements with up to 16^3 Gauss–Lobatto–Legendre (GLL) grid points within each element. This gives a total of ≈ 908 million grid points per simulation. We enforce a no-slip condition at the bottom boundary for the velocity field and a zero gradient in the wall-normal direction for the concentration field. At the top ($z = 20$) and the outflow ($x = 96\pi$) boundaries we use open boundary conditions (45).

The inlet velocity, concentration, and turbulence structure are obtained by performing an auxiliary highly resolved direct numerical simulation of a turbidity current with a roof (25) on a channel of height 2H over a bed inclined at an angle θ (see parabolic profile of streamwise velocity at inlet in Fig. 1*C*).

The vortical structures of the flow are obtained by computing the swirling strength λ_{ci}, defined as the absolute value of the imaginary portion of the complex eigenvalues of the local velocity gradient tensor $\nabla \mathbf{u}$ (27, 46). The velocity gradient tensor has three eigenvalues. If one of the eigenvalues is real, the other two are complex conjugates and $\lambda_{ci} \neq 0$. The case of $\lambda_{ci} = 0$ corresponds to locations where all eigenvalues of $\nabla \mathbf{u}$ are real. This method provides a clean and selective measure of the vortical structures as it discriminates the regions with planar shear. Code is available at https://nek5000.mcs.anl.gov/. Simulation data are available to the reader at https://osf.io/x9vw4/.

ACKNOWLEDGMENTS. We thank ExxonMobil for their support. J.S. and M.C. also acknowledge Consejo Nacional de Investigaciones Científicas y Técnicas, Comisión Nacional de Energía Atómica, and Universidad Nacional de Cuyo.

1. J. Fan, G. L. Morris, Reservoir sedimentation. II: Reservoir desiltation and long-term storage capacity. *J. Hydraul. Eng.* **118**, 370–384 (1992).
2. T. Salaheldin, J. Imran, M. Chaudhry, C. Reed, Role of fine-grained sediment in turbidity current flow dynamics and resulting deposits. *Mar. Geol.* **171**, 21–38 (2000).
3. E. Meiburg, B. Kneller, Turbidity currents and their deposits. *Annu. Rev. Fluid Mech.* **42**, 135–156 (2010).
4. P. J. Talling *et al.*, Onset of submarine debris flow deposition far from original giant landslide. *Nature* **450**, 541–544 (2007).
5. C. Pirmez, J. Imran, Reconstruction of turbidity currents in Amazon channel. *Mar. Petrol. Geol.* **20**, 823–849 (2003).
6. R. F. Sánchez-Leal *et al.*, The Mediterranean overflow in the Gulf of Cadiz: A rugged journey. *Sci. Adv.* **3**, eaao0609 (2017).
7. P. J. Talling *et al.*, Key future directions for research on turbidity currents and their deposits. *J. Sediment. Res.* **85**, 153–169 (2015).
8. G. Parker, M. Garcia, Y. Fukushima, W. Yu, Experiments on turbidity currents over an erodible bed. *J. Hydraul. Res.* **25**, 123–147 (1987).
9. B. Launder, W. Rodi, The turbulent wall jet. *Prog. Aerosp. Sci.* **19**, 81–128 (1979).
10. A. Sigalla, Measurements of skin friction in a plane turbulent wall jet. *J. R. Aeronaut. Soc.* **62**, 873–877 (1958).
11. O. E. Sequeiros, Estimating turbidity current conditions from channel morphology: A Froude number approach. *J. Geophys. Res. Oceans* **117**, C04003 (2012).
12. O. E. Sequeiros *et al.*, Characteristics of velocity and excess density profiles of saline underflows and turbidity currents flowing over a mobile bed. *J. Hydraul. Eng.* **136**, 412–433 (2010).
13. J. S. Salinas, M. Shringarpure, M. Cantero, S. Balachandar, Properties of the body of a turbidity current at near normal conditions: 1. Effect of bed slope. *J. Geophys. Res. Oceans* **124**, 7989–8016 (2019).
14. T. Ellison, J. Turner, Turbulent entrainment in stratified flows. *J. Fluid Mech.* **6**, 423–448 (1959).
15. H. Huang, J. Imran, C. Pirmez, Q. Zhang, G. Chen, The critical densimetric Froude number of subaqueous gravity currents can be non-unity or non-existent. *J. Sediment. Res.* **79**, 479–485 (2009).
16. E. Sumner *et al.*, First direct measurements of hydraulic jumps in an active submarine density current. *Geophys. Res. Lett.* **40**, 5904–5908 (2013).
17. M. A. Islam, J. Imran, Vertical structure of continuous release saline and turbidity currents. *J. Geophys. Res. Oceans* **115**, C08025 (2010).
18. M. I. Cantero *et al.*, Emplacement of massive turbidities linked to extinction of turbulence in turbidity currents. *Nat. Geosci.* **5**, 42–45 (2012).
19. M. I. Cantero, S. Balachandar, A. Cantelli, G. Parker, A simplified approach to address turbulence modulation in turbidity currents as a response to slope breaks and loss of lateral confinement. *Environ. Fluid Mech.* **14**, 371–385 (2014).
20. Z. Nourmohammadi, H. Afshin, B. Firoozabadi, Experimental observation of the flow structure of turbidity currents. *J. Hydraul. Res.* **49**, 168–177 (2011).
21. E. Khavasi, H. Afshin, B. Firoozabadi, Effect of selected parameters on the depositional behaviour of turbidity currents. *J. Hydraul. Res.* **50**, 60–69 (2012).
22. K. Taki, G. Parker, Transportational cyclic steps created by flow over an erodible bed. Part 1. Experiments. *J. Hydraul. Res.* **43**, 488–501 (2005).
23. S. Kostic, O. Sequeiros, B. Spinewine, G. Parker, Cyclic steps: A phenomenon of supercritical shallow flow from the high mountains to the bottom of the ocean. *J. Hydro-environment Res.* **3**, 167–172 (2010).
24. A. Fildani, W. R. Normark, S. Kostic, G. Parker, Channel formation by flow stripping: Large-scale scour features along the Monterey east channel and their relation to sediment waves. *Sedimentology* **53**, 1265–1287 (2006).
25. M. I. Cantero, S. Balachandar, A. Cantelli, C. Pirmez, G. Parker, Turbidity current with a roof: Direct numerical simulation of self-stratified turbulent channel flow driven by suspended sediment. *J. Geophys. Res. Oceans* **114**, C03008 (2009).
26. M. Shringarpure, M. I. Cantero, S. Balachandar, Dynamics of complete turbulence suppression in turbidity currents driven by monodisperse suspensions of sediment. *J. Fluid Mech.***712**, 384–417 (2012).
27. P. Chakraborty, S. Balachandar, R. Adrian, On the relationships between local vortex identification schemes. *J. Fluid Mech.* **535**, 189–214 (2005).
28. D. H. Richter, P. P. Sullivan, Modification of near-wall coherent structures by inertial particles. *Phys. Fluids* **26**, 103304 (2014).
29. M. I. Cantero, S. Balachandar, M. Garcia, D. Bock, Turbulent structures in planar gravity currents and their influence of the flow dynamics. *J. Geophys. Res. Oceans* **113**, C08018 (2008).
30. M. H. Garcia, "Depositing and eroding sediment-driven flows: turbidity currents," PhD thesis, University of Minnesota, St. Anthony Falls Hydraulic Laboratory, MN (1990).
31. M. García, G. Parker, Experiments on the entrainment of sediment into suspension by a dense bottom current. *J. Geophys. Res.* **98**, 4793–4807 (1993).
32. B. Kneller, M. M. Nasr-Azadani, S. Radhakrishnan, E. Meiburg, Long-range sediment transport in the world's oceans by stably stratified turbidity currents. *J. Geophys. Res. Oceans* **121**, 8608–8620 (2016).
33. J. S. Salinas, M. Shringarpure, M. Cantero, S. Balachandar, Properties of the body of a turbidity current at near normal conditions: 2. Effect of settling. *J. Geophys. Res. Oceans* **124**, 8017–8035 (2019).
34. M. García, "Experimental study of turbidity currents," Ms thesis, University of Minnesota, Minneapolis, MN (1985).
35. X. Wu, P. Moin, Direct numerical simulation of turbulence in a nominally zero-pressure-gradient flat-plate boundary layer. *J. Fluid Mech.* **630**, 5–41 (2009).
36. G. Parker, Y. Fukushima, H. Pantin, Self-accelerating turbidity currents. *J. Fluid Mech.* **171**, 145–181 (1986).
37. C. R. Meyer, P. Linden, Stratified shear flow: Experiments in an inclined duct. *J. Fluid Mech.* **753**, 242–253 (2014).
38. A. Lefauve, J. Partridge, P. Linden, Regime transitions and energetics of sustained stratified shear flows. *J. Fluid Mech.* **875**, 657–698 (2019).
39. J. W. Miles, On the stability of heterogeneous shear flows. *J. Fluid Mech.* **10**, 496–508 (1961).
40. T. Sun, G. Parker, Transportational cyclic steps created by flow over an erodible bed. Part 2. Theory and numerical simulation. *J. Hydraul. Res.* **43**, 502–514 (2005).
41. J. J. Fedele, D. Hoyal, Z. Barnaal, J. Tulenko, S. Awalt, "Bedforms created by gravity flows" in *Autogenic Dynamics and Self-Organization in Sedimentary Systems*, D. A. Budd, E. A. Hajek, S. J. Purkis, Eds. (SEPM Society for Sedimentary Geology, 2016) pp. 95–121.
42. J. E. H. Clarke, First wide-angle view of channelized turbidity currents links migrating cyclic steps to flow characteristics. *Nat. Commun.* **7**, 11896 (2016).
43. A. T. Patera, A spectral element method for fluid dynamics: Laminar flow in a channel expansion. *J. Comput. Phys.* **54**, 468–488 (1984).
44. M. O. Deville, P. F. Fischer, P. F. Fischer, E. Mund, *High-Order Methods for Incompressible Fluid Flow* (Cambridge University Press, 2002), vol. 9.
45. F. Q. Hu, On absorbing boundary conditions for linearized Euler equations by a perfectly matched layer. *J. Comput. Phys.* **129**, 201–219 (1996).
46. J. Zhou, R. Adrian, S. Balachandar, T. Kendall, Mechanics for generating coherent packets of hairpin vortices in channel flow. *J. Fluid Mech.* **387**, 353–396 (1999).